Gradient-dependent exchange-correlation kernel for materials optical properties

Aleksandr V. Terentjev,[1] Lucian A. Constantin,[2] and J. M. Pitarke[3,4]

[1]*Donostia International Physics Center (DIPC), E-20018 Donostia, Basque Country, Spain*

[2]*Center for Biomolecular Nanotechnologies @UNILE, Istituto Italiano di Tecnologia, Via Barsanti, I-73010 Arnesano, Italy*

[3]*CIC nanoGUNE, Tolosa Hiribidea 76, E-20018 Donostia, Basque Country, Spain*

[4]*Materia Kondentsatuaren Fisika Saila, Centro Física Materiales CSIC-UPV/EHU, and DIPC, 644 Posta kutxatila,*
E-48080 Bilbo, Basque Country, Spain

We have developed an exchange-correlation kernel in the framework of time-dependent density-functional theory that remarkably accounts for the electron-hole interaction and the optical properties of semiconductors. This kernel, which we name JGM-G, generalizes the jellium-with-gap kernel of Trevisanutto *et al.* [Phys. Rev. B **87**, 205143 (2013)] by considering the gradient of the density as a new ingredient. We have tested it on various materials, from low-band-gap to wide-band-gap semiconductors, and we have demonstrated that the JGM-G kernel yields an optical response that is close to experiment. These encouraging results indicate that the JGM-G kernel can become a low-cost and practical tool for the description of excitonic effects in semiconductors.

I. INTRODUCTION

In the framework of time-dependent density-functional theory (TDDFT), the *exact* density-response function of a many-electron system is found to be given by the following Dyson-like expression (in atomic units) [1]:

$$\chi(\mathbf{r}, \mathbf{r}'; \omega) = \chi^0(\mathbf{r}, \mathbf{r}'; \omega) + \int d\mathbf{r}_1 \, d\mathbf{r}_2 \, \chi^0(\mathbf{r}, \mathbf{r}_1; \omega)$$
$$\times v_{\text{eff}}[n](\mathbf{r}_1, \mathbf{r}_2; \omega) \, \chi(\mathbf{r}_2, \mathbf{r}'; \omega), \quad (1)$$

where $\chi^0(\mathbf{r}, \mathbf{r}'; \omega)$ is the noninteracting density-response function of Kohn-Sham electrons at frequency ω and $v_{\text{eff}}[n](\mathbf{r}_1, \mathbf{r}_2; \omega)$ represents an effective electron-electron interaction:

$$v_{\text{eff}}[n](\mathbf{r}, \mathbf{r}'; \omega) = \frac{1}{|\mathbf{r} - \mathbf{r}'|} + f_{xc}[n](\mathbf{r}, \mathbf{r}'; \omega), \quad (2)$$

with $f_{xc}[n](\mathbf{r}, \mathbf{r}'; \omega)$ being the so-called exchange-correlation (XC) kernel. The macroscopic dielectric function of the many-electron system is obtained as follows

$$\epsilon^M(\mathbf{q}, \omega) = 1/\epsilon^{-1}_{\mathbf{G}=\mathbf{G}'=0}(\mathbf{q}, \omega), \quad (3)$$

where

$$\epsilon^{-1}_{\mathbf{G}, \mathbf{G}'}(\mathbf{q}, \omega) = \delta_{\mathbf{G}, \mathbf{G}'} + v_{\mathbf{q}+\mathbf{G}} \, \chi_{\mathbf{G}, \mathbf{G}'}(\mathbf{q}, \omega). \quad (4)$$

Here, q represents a wave vector in the first Brillouin zone, $v_{\mathbf{k}}$ is the Fourier transform of the bare Coulomb interaction $1/|\mathbf{r} - \mathbf{r}'|$, and $\chi_{\mathbf{G}, \mathbf{G}'}(\mathbf{q}, \omega)$ represent the Fourier coefficients of the density-response function of Eq. (1), $\mathbf{G}$ and $\mathbf{G}'$ being reciprocal lattice vectors.

The optical response of an arbitrary many-electron system is obtained from the $q \to 0$ limit of the macroscopic dielectric function of Eq. (3). On the other hand, the *exact* XC energy of an arbitrary many-electron system can be obtained by using the adiabatic-connection fluctuation-dissipation theorem (ACFDT) [2,3], from the knowledge of a density-response function of the form of Eq. (1) with the full electron-electron coupling strength e^2 being replaced by a coupling strength λe^2 with λ varying from 0 to 1. Both the ground-state energy and the optical response call for the knowledge of the XC kernel entering Eq. (2). In the random-phase approximation (RPA), this kernel is simply taken to be zero. However, although RPA is accurate for many ground-state properties [4–19] it fails to describe excitons at insulators and semiconductors.

The success of the so-called Nanoquanta XC kernel [20,21], derived from the Bethe-Salpeter equation [22], proved that TDDFT can be used for the computation of the optical properties of all kinds of materials. This accurate XC kernel has, however, a very high computational cost, comparable to solving the Bethe-Salpeter equation itself. Nowadays, there is an intense ongoing research for the development of low-cost XC kernels capable of describing excitonic effects of real solids [23–36]. Among others, we have the Bootstrap (iteration) kernel [23], the long-range contribution (LRC) kernel [37,38] and its simplifications/improvements [29,31], as well as a kernel that is based on a jellium-with-gap model (JGM) [33]. All these kernels take into account the ultra-nonlocality effect: an exact property derived from the zero-force theorem [39,40], which happens to be crucial for the description of excitonic effects. Another XC kernel that can well describe the optical properties of materials [36] is a simple and nonempirical dynamical polarization functional derived from the Vignale-Kohn functional [41], in the context of time-dependent current density-functional theory (TDCDFT) [34,41,42].

In this paper, we present an XC kernel: JGM-G, which improves over the JGM kernel by introducing the density gradient ∇n as a variable in addition to the density n and the fundamental band gap E_g. The JGM-G kernel is simpler than JGM but more powerful because of the ∇n dependence, and it is found to be remarkably accurate for the description of the optical properties of a great variety of semiconductors. The paper is organized as follows. In Sec. II, we introduce

the theoretical development of our JGM-G XC kernel. The computational details are reported in Sec. III. In Sec. IV, we show and discuss our results for the so-called macroscopic dielectric function ϵ^M (both $\Re\epsilon^M$ and $\Im\epsilon^M$) of a large palette of bulk materials. In Sec. V, we summarize our main results and present our conclusions.

II. CONSTRUCTION OF THE JGM-G EXCHANGE-CORRELATION KERNEL

The JGM XC kernel [33] was constructed from the Constantin-Pitarke (CP) static XC kernel of a uniform electron gas [43], by incorporating the ultra-nonlocality condition derived from a jellium-with-gap model system [33,44]. This kernel has, in momentum space, the following jelliumlike sophisticated expression [33]:

$$f_{xc}^{\text{JGM}}(q; n, E_g) = \frac{4\pi}{q^2} B'(n, E_g)[e^{-k'_{n,E_g}q^2} - 1]$$
$$- \frac{4\pi}{k_F^2} \frac{C'(n, E_g)}{1 + 1/q^2}, \quad (5)$$

where E_g represents the fundamental band gap,

$$B'(n, E_g) = \frac{B(n) + E_g}{1 + E_g}, \quad C'(n, E_g) = \frac{C(n)}{1 + E_g},$$
$$(6)$$
$$k'_{n,E_g} = k_n + \frac{1}{4\pi q^2} \frac{E_g^2}{n B'(n, E_g)},$$

and

$$k_n = -\frac{1}{4\pi} \frac{d^2}{dn^2}[n\epsilon_{xc}(n)], \quad (7)$$

with $\epsilon_{xc} = \epsilon_x + \epsilon_c$ being the XC energy per particle of the uniform electron gas which we obtain from the Perdew-Wang parametrization [45]. k_F represents the magnitude of the Fermi wave vector, and [43]

$$B(n) = \frac{1 + 2.15r_s^{1/2} + 0.435r_s^{3/2}}{3 + 1.57r_s^{1/2} + 0.409r_s^{3/2}},$$
$$(8)$$
$$C(n) = -\frac{\pi}{2k_F} \frac{d(r_s\epsilon_c)}{dr_s}.$$

Here $r_s = (3/4\pi n)^{1/3}$ is the bulk parameter.

The last term of Eq. (5), which yields a complicated real-space expression (see Eq. [A5] of Ref. [43]), does not play a role in the description of the optical response dictated by the $q \to 0$ limit. Thus, Patrick and Thygesen [46] proposed the following simplified version of the JGM kernel, named JGMs:

$$f_{xc}^{\text{JGMs}}(q; n, G) = \frac{4\pi}{q^2}[e^{-k_n q^2} e^{-G^2/(4\pi n)} - 1], \quad (9)$$

with $G = E_g$. This simplified kernel is remarkably accurate for the description of a uniform electron gas [15] and also for the description of a number of ground-state properties of bulk solids [46] (equilibrium lattice constants, bulk moduli, and correlation energies). Moreover, this kernel preserves the ultra-nonlocality condition fulfilled by the original JGM kernel:

$$f_{xc}^{\text{JGMs}}(q \to 0; n, E_g) = f_{xc}^{\text{JGM}}(q \to 0; n, E_g) = -\frac{E_g^2}{nq^2},$$
$$(10)$$

and agrees well with original JGM kernel when $q \lesssim 1$ (see Fig. 1 of Ref. [43]) so the kernels JGM and JGMs yield *practically* the same optical properties. The real-space representation of JGMs is [46]:

$$f_{xc}^{\text{JGMs}}(R) = \frac{1}{R}\left[e^{-G^2/(4\pi n)}\text{erf}\left(\frac{R}{2\sqrt{k_n}}\right) - 1\right], \quad (11)$$

with $R = |\mathbf{r} - \mathbf{r}'|$ and erf(x) the error function. When $G = 0$, Eq. (11) yields the CP kernel [15,43].

For a JGM-G kernel with a density gradient, we still use Eq. (11) but with $G = E_g$ being now replaced by

$$G = E_g f(n, \nabla n), \quad (12)$$

so when $E_g = 0$ the JGM-G kernel still recovers the simplified CP kernel, which, as in the ALDA, can accurately account for the optical properties of metals [47]. For the function $f(n, \nabla n)$, we propose the following heuristic expression for bulk solids:

$$f(n, \nabla n) = \frac{a}{\frac{1}{V}\int_V d\mathbf{r} \frac{|\nabla n|^2}{n^2}} \frac{|\nabla n|^4}{n^4}, \quad (13)$$

where a is a non-negative parameter ($a \geqslant 0$). We recall that averages over the unit cell have also been used, with good results, in the development of a kinetic-energy functional for an orbital-free DFT [48], and especially in the construction of the MBJ semilocal exchange potential that is accurate for the study of band gap energies of solids [49]. Moreover, the ratio $|\nabla n|/n$ is an important density indicator, being used in hybrid functionals with local range separation [50], in the MBJ semilocal exchange potential construction [49], and in local band gap models [51,52].

We fix the parameter $a = 0.46$, in such a way that the JGM-G kernel yields optical absorption spectra of the low-band-gap semiconductors InSb ($E_g = 0.23$ eV) and InAs ($E_g = 0.43$ eV) that coincide with the optical absorption spectra obtained with the JGM or JGMs kernel. This condition ensures that at low values of E_g the JGM-G kernel converges with JGM and JGMs. This completes the construction of our kernel JGM-G.

In the case of finite systems, the tail of the electron density decays as [53] $n \sim e^{-2\sqrt{2I}r}$, with I being the ionization potential (in absolute value). Equation (12) then becomes

$$G = \frac{E_g}{I} \frac{a}{8} \frac{|\nabla n|^4}{n^4}. \quad (14)$$

Let us consider, in particular, jellium clusters, as they represent important model systems in solid-state physics. We recall that a neutral jellium cluster with N electrons and bulk parameter r_s has the radius $R_c = r_s N^{1/3}$ and the external potential

$$V_{\text{ext}}(\mathbf{r}) = \begin{cases} N\left(-\frac{3}{2R_c} + \frac{r^2}{2R_c^3}\right), & r < R_c \\ -N\frac{1}{r}, & r \geqslant R_c \end{cases} \quad (15)$$

due to a positive background density

$$n_+(\mathbf{r}) = \begin{cases} 3/4\pi r_s^3 & r < R_c \\ 0 & r \geqslant R_c \end{cases}. \quad (16)$$

Even for intermediate values of N (e.g., $N \geqslant 58$), inside the cluster radius (i.e., when $r \leqslant R_c$) the density varies slowly so jellium-based XC kernels are accurate.
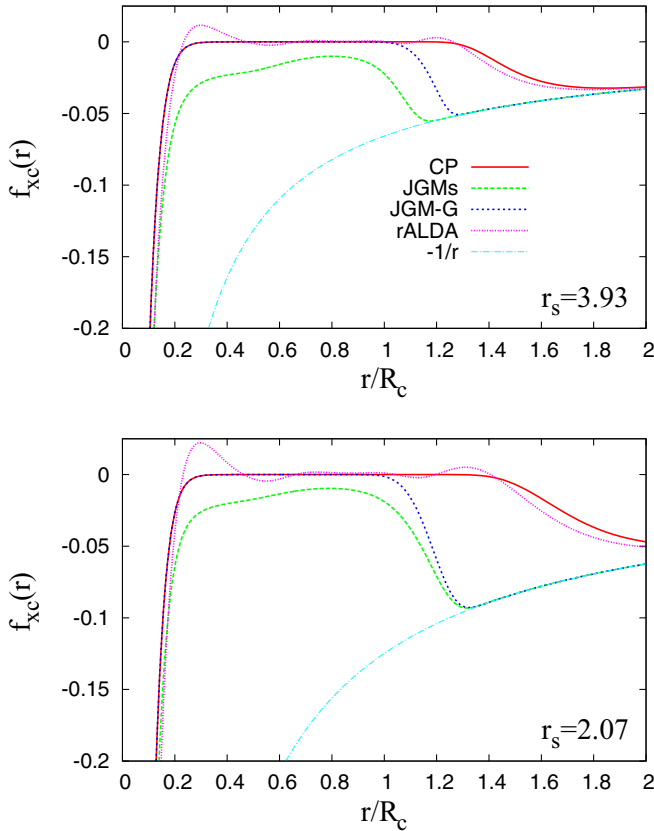
FIG. 1. The real-space XC kernels (simplified CP, JGMs, JGM-G, rALDA [46,54–56]) for jellium spheres with $N = 58$ electrons, and $r_s = 3.93$ (upper panel), and $r_s = 2.07$ (lower panel), versus the scaled radial distance r/R_c. Note that $r_s = 3.93$ corresponds to Na, and $r_s = 2.07$ to Al.

In Fig. 1, we show several XC kernels $f_{xc}(r)$, with r being the radial distance of jellium spheres, for $N = 58$ electrons and $r_s = 3.93$ and 2.07. The calculations have been performed with the Engel code [57,58], using LDA orbitals and densities. The band gap used in JGMs and JGM-G has been obtained as $E_g = I - A = [E(N - 1) - E(N)] - [E(N) - E(N + 1)]$. The CP and rALDA kernels agree well everywhere, but the rALDA kernel shows more structure and small oscillations. As expected, the JGM-G kernel nicely recovers the CP kernel in the interior of the sphere (at $r \leqslant R_c$), thus correcting over the JGMs kernel. At $r \geqslant R_c$, the JGM-G coincides with JGMs kernel, thus recovering the $-1/r$ limit faster than in the case of the CP and rALDA kernels. Hence, due to its density-gradient dependence, our JGM-G kernel is able to distinguish regions where the density varies slowly or rapidly.

III. COMPUTATIONAL DETAILS

For the evaluation of the macroscopic dielectric function ϵ^M, we first compute the eigenvalues and eigenfunctions of a single-particle Kohn-Sham Hamiltonian in the framework of density-functional theory (DFT) by using the QE package (V5.3, Quantum Espresso Foundation, Cambridge, UK) [59] with PBE Trouiller-Martins norm-conserving pseudopotentials including sp electrons only as valence electrons, as for the energies under study this is enough for the description

of the optical response of bulk materials. We have used the following Monkhorst-Pack k-point meshes: $24 \times 24 \times 24$ for InSb, InAs, Ge, InP, AlAs, and GaP, and $32 \times 32 \times 32$ for the remaining systems. An energy cutoff of 150 Ry was used for InAs and MgO, 160 Ry for InP, 180 Ry for LiF, and 120 Ry for the remaining systems.

For the calculation of the macroscopic dielectric function ϵ^M the Yambo code [60] was used, after implementation of the JGMs kernel and our JGM-G kernel as well. Our full calculations were performed with reciprocal-space matrices of size N_G for both f_{xc} and the density-response function: $N_G = 307$ for MgO and LiF, and $N_G = 113$ for the remaining systems. We first derive the Fourier coefficients of the XC kernel of Eq. (9) [or Eq. (11)], which we then use to obtain [by solving Eq. (1) in reciprocal space] the Fourier coefficients $\chi_{\mathbf{G},\mathbf{G}'}$ entering Eq. (4).

For an accurate description of the band structure, we calculate the noninteracting Kohn-Sham density-response function χ^0 in the framework of a scissor-operator corrected DFT with $E^{SO} = E_g^{EXP} - E_g^{DFT}$, E_g^{EXP} being the experimental fundamental band gap also used in the construction of the kernels JGMs and JGM-G. Instead, one can use the so-called GW approximation of many-body theory, but the use, in the framework of DFT, of a scissor operator yields the same results for the optical response, as already shown in the literature [21,23,33,37,38]. Accurate band-gap energies can also be obtained from semilocal DFT approaches [49].

IV. RESULTS

In the optical limit of long wavelengths, one writes the real and the imaginary part of the macroscopic dielectric function ϵ^M as follows

$$\epsilon_1(\omega) = \Re\Big[\lim_{q \to 0} \epsilon^M(q, \omega) \Big],$$
$$\epsilon_2(\omega) = \Im\Big[\lim_{q \to 0} \epsilon^M(q, \omega) \Big]. \tag{17}$$

The optical absorption spectrum is simply dictated by ϵ_2, the Fresnel reflectivity at normal incidence is $R(\omega) = |(\sqrt{\epsilon(\omega)} - 1)/(\sqrt{\epsilon(\omega)} + 1)|^2$, and the long-wavelength limit of the electron-energy-loss function is equal to $\epsilon_2(\omega)/[\epsilon_1(\omega)^2 + \epsilon_2(\omega)^2]$.

In this section, we show both $\epsilon_1(\omega)$ and $\epsilon_2(\omega)$ for a large variety of semiconductors and insulators (InSb, InAs, Ge, GaSb, Si, GaAs, InP, AlAs, GaP, SiC, AlP, and diamond), whose band-gap energies lay between 0.23 eV and 5.48 eV, and we also report the optical absorption spectra of the wide-band-gap insulators MgO and LiF. Experimental lattice constants with zero-point energy (ZPE) corrections are taken from Ref. [13] for all materials except GaSb. For GaSb, the experimental lattice constant (with no ZPE correction) is taken from Ref. [61].

The experimental $\epsilon_1(\omega)$ and $\epsilon_2(\omega)$ are both known to be sensitive to the temperature. In particular, the intensity of the first optical-absorption peak increases significantly when the temperature decreases from ≈ 300 K to below 100 K, as shown for Si in Fig. 4 of Ref. [62], for Ge in Fig. 2 of Ref. [63], and for GaP in Fig. 3 of Ref. [64]. In all these cases, the absorption peaks are also blueshifted as temperature decreases. Thus,
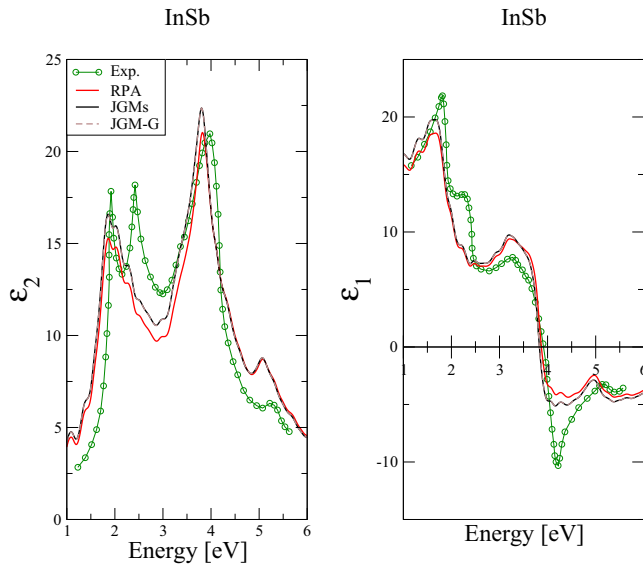
FIG. 2. $\epsilon_1(\omega)$ and $\epsilon_2(\omega)$ computed in the linear-response TD-DFT, from several XC kernels (RPA, JGMs, and JGM-G) versus ω, for the InSb low-gap semiconductor ($E_g = 0.23$ eV [67]). The experimental curves are from Ref. [66] (at $T = 100$ K). The results are obtained with Lorentzian broadening of 0.1.

we compare our calculations with experimental data obtained at the lowest possible temperature. In all figure captions, we report the experimental temperature. For InAs, SiC, AlP, diamond, MgO and LiF, we use experimental data obtained at room temperature. In the case of diamond, temperature effects are known to be nearly negligible [65]. For SiC [38], MgO [33,38], and LiF [20] the Bethe-Salpeter results agree well with experiment, so temperature effects for these materials are also expected to be small.
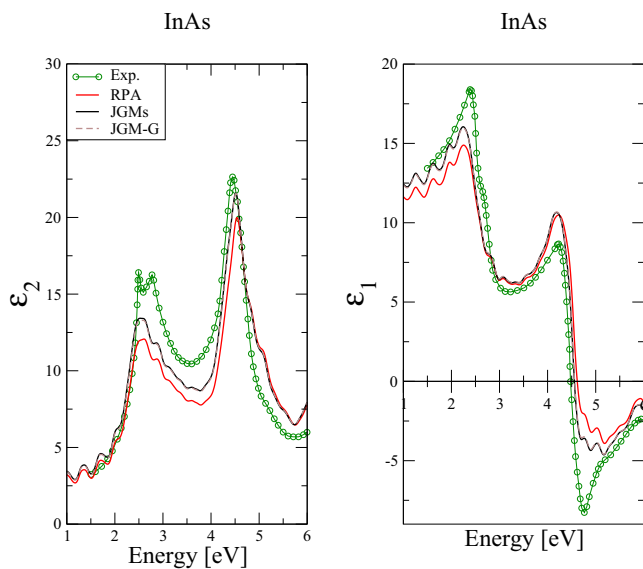

FIG. 3. Same as Fig. 2 but for the InAs low-gap semiconductor ($E_g = 0.43$ eV [67]). The experimental curves are from Ref. [70] (at room temperature). The results are obtained with Lorentzian broadening of 0.1.

A. Indium antimonide (InSb)

In the case of low-band-gap semiconductors, the electron-hole (e-h) interaction has an impact on the spectral weight of the excitations. In order to measure this spectral weight, we consider the following ratio:

$$\zeta_2 = \frac{\epsilon_2(\omega_l)}{\epsilon_2(\omega_f)}, \qquad (18)$$

where ω_l and ω_f represent the energies of the last and first peaks of the absorption spectrum, respectively.

In Fig. 2, we show $\epsilon_1(\omega)$ and $\epsilon_2(\omega)$ as obtained in the RPA and with the use of the XC kernels JGMs and JGM-G. For this low-band-gap semiconductor, $\epsilon_1(\omega)$ and $\epsilon_2(\omega)$ are not sensitive to whether the kernel JGMs or the kernel JGM-G is used in our calculations: Both results are indistinguishable to the naked eye. The RPA is also rather accurate, but the use of the XC kernel JGMs or JGM-G clearly improves the ratio ζ_2: $\zeta_2^{RPA} \sim$ 1.4, $\zeta_2^{JGMs} = \zeta_2^{JGM-G} \sim 1.3$, and $\zeta_2^{exp} \sim 1.2$. This brings us to the conclusion that the use of both JGMs and JGM-G kernels yields a description of the main excitonic peak at 4 eV that is more realistic than in the RPA. The two consecutive peaks of the experimental absorption spectra at $\sim$2 and 2.5 eV, which are not present in our calculations, are due to a large spin-orbit splitting [68] not considered here.

In the case of $\epsilon_1(\omega)$, both the RPA and the use of the kernels JGMs and JGM-G yield good results in close agreement with experiment in the entire range of energies under study (from 0 to 6 eV). We note that the results obtained by using the kernels JGMs and JGM-G are overall slightly superior to the RPA calculation. An accurate description of InSb is important, as it is used in infrared detectors, including thermal imaging cameras, in forward looking infrared (FLIR) systems, and in other optical devices [69].

B. Indium arsenide (InAs)

In Fig. 3, we show $\epsilon_1(\omega)$ and $\epsilon_2(\omega)$ for the low-band-gap semiconductor InAs. As in the case of InSb, the JGMs and JGM-G curves are indistinguishable and they both improve the ratio ζ_2 over the RPA: $\zeta_2^{RPA} \sim 1.7$, $\zeta_2^{JGMs} = \zeta_2^{JGM-G} \sim 1.6$, and $\zeta_2^{exp} \sim 1.4$. Also as in InSb, the two consecutive peaks of the experimental absorption spectra at $\sim$2.5 and 2.8 eV are due to a large spin-orbit splitting [68] not considered here, and the results we obtain by using the kernels JGMs and JGM-G are here also superior to the RPA calculation in that they yield $\epsilon_1(\omega) = 0$ at an energy that is closer to experiment by 0.05 eV, although still another 0.05 eV higher than the experimental value. InAs, like InSb, has applications in various infrared optical devices [71].

C. Germanium (Ge)

In Ge, as in InSb and InAs, $\epsilon_1(\omega)$ and $\epsilon_2(\omega)$ are not sensitive to whether the JGMs kernel or the JGM-G kernel is used in our calculations (see Fig. 4) and both kernels improve considerably the ratio ζ_2 over the RPA: $\zeta_2^{RPA} \sim 1.6$, $\zeta_2^{JGM-G} \sim 1.4$, $\zeta_2^{JGMs} \sim$ 1.35, and $\zeta_2^{exp} \sim 1.3$. The results we obtain by using the kernels JGMs and JGM-G are here also superior to the RPA calculation in that they yield $\epsilon_1(\omega) = 0$ at an energy that is closer to experiment by 0.05 eV, although still 0.1 eV higher than the
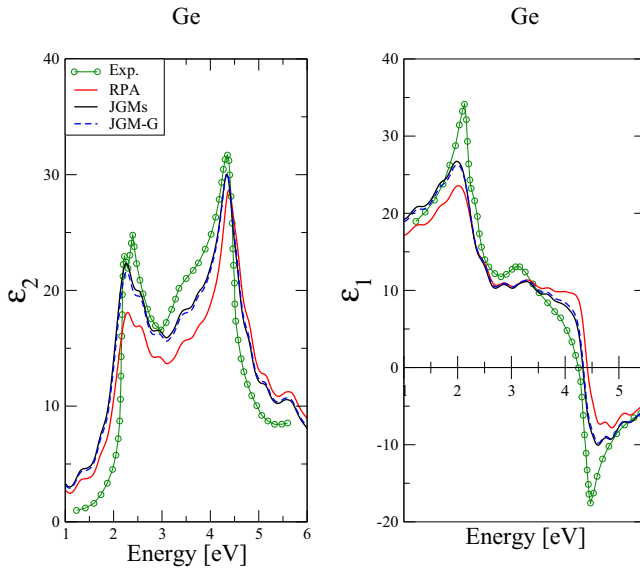
FIG. 4. Same as Fig. 2 but for the Ge low-gap semiconductor ($E_g = 0.74$ eV [49]). The experimental curves are from Ref. [63] (at $T = 100$ K). The results are obtained with Lorentzian broadening of 0.15.

FIG. 6. Same as Fig. 2 but for the Si semiconductor ($E_g = 1.17$ eV [49]). The experimental curves are from Ref. [62] (at $T = 30$ K). The results are obtained with Lorentzian broadening of 0.1.

experimental value. Germanium optical components are used in many infrared applications, including, for example, thermal imaging and spectroscopy [72].

D. Gallium antimonide (GaSb)

The results we have obtained for GaSb are shown in Fig. 5. As before, $\epsilon_1(\omega)$ and $\epsilon_2(\omega)$ are not sensitive to whether the JGMs kernel or the JGM-G kernel is used in our calculations. Overall, both kernels give a realistic description of ϵ_1 and ϵ_2, considerably improving over RPA calculations. The calculated optical absorption spectra exhibits an averaged, rounded peak

at about 2.5 eV instead of the two consecutive experimental peaks at 2.2 and 2.6 eV, which as in the case of InSb and InAs are the result of a spin-orbit splitting [68] not included in our calculations.

As for the energy at which $\epsilon_1(\omega) = 0$, both JGMs and JGM-G calculations are blueshifted by 0.25 eV with respect to the experimental data, but they are closer to experiment than in the RPA. We also note that there is a weak structure in ϵ_2 at 5–6 eV that is present in all our calculations, no matter whether the XC kernel is taken to be zero (RPA) or not. GaSb is used for infrared detectors, infrared LEDs, and thermophotovoltaic systems [72].

E. Silicon (Si)

Silicon is one of the most important materials in current technologies and represents a difficult test in the assessment of theoretical methods for the description of the optical properties of a variety of materials. Electron-hole interactions are more pronounced in Si than in the low-band-gap semiconductors discussed above. As a result, the RPA fails to realistically describe ϵ_1 and ϵ_2 in Si, as can be seen in Fig. 6.

In Si, the introduction of the density gradient in Eq. (12) considerably improves both ϵ_1 and ϵ_2, i.e., the spectra one obtains by using the XC kernel JGM-G is considerably superior to that obtained with the use of JGMs. The introduction of the density gradient appears to be particularly important for the description of the oscillator strength associated to the peak at 3.4 eV. The accuracy we reach with the use of the XC kernel JGM-G is comparable to, or even better than, the accuracy one obtains with the use of other low-cost methods such as the Bootstrap self-consistent scheme [23] and a meta-generalized gradient approximation (meta-GGA) [32], although still worse than the result one obtains with the use of a dynamical polarization functional [36].
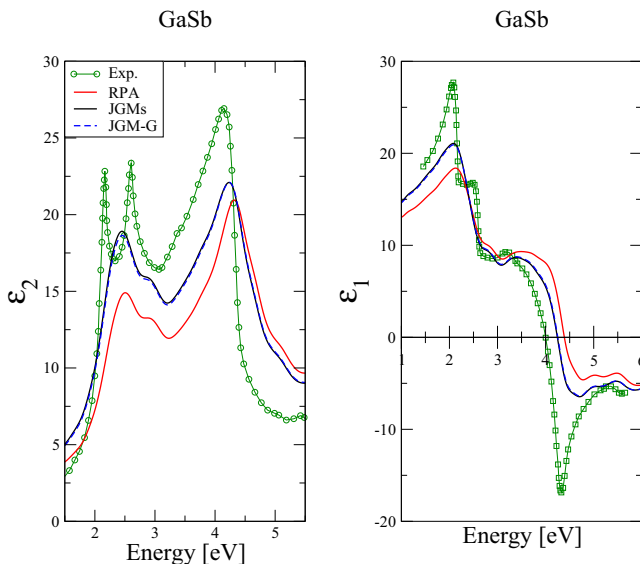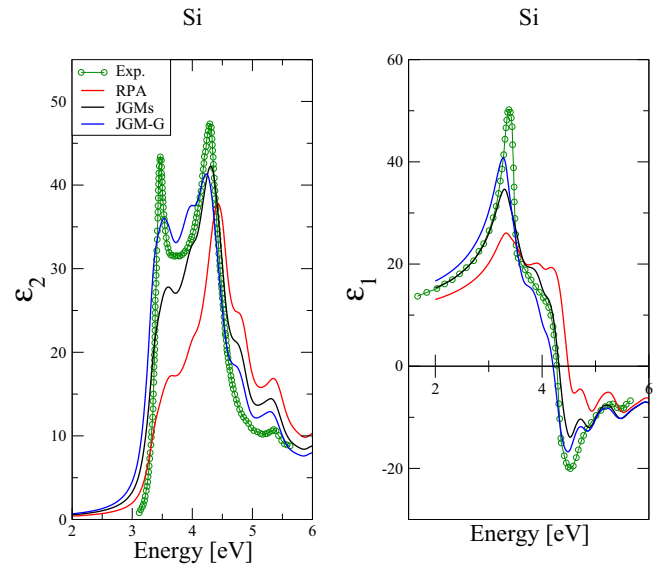

FIG. 5. Same as Fig. 2 but for the GaSb semiconductor ($E_g = 0.81$ eV [67]). The experimental curves are from Ref. [73] (at $T = 10$ K). The results are obtained with Lorentzian broadening of 0.2.
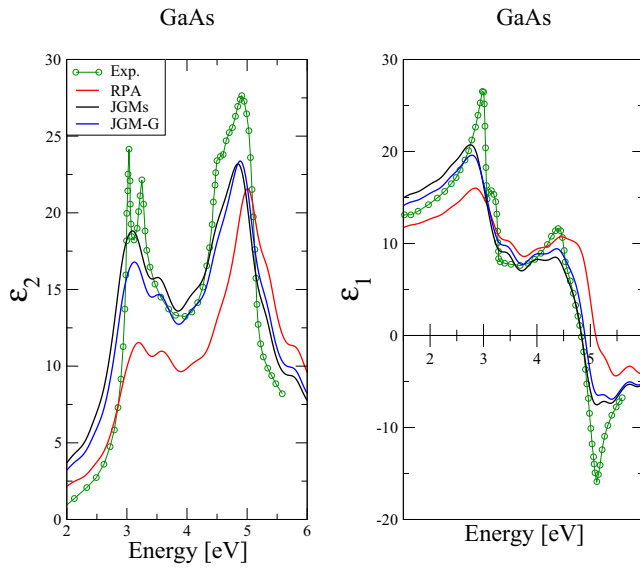
FIG. 7. Same as Fig. 2 but for the GaAs semiconductor ($E_g = 1.42$ eV [67]). The experimental curves are from Ref. [78] (at $T = 22$ K). The results are obtained with Lorentzian broadening of 0.2.

The use of our kernel JGM-G yields a significant improvement over the use of JGMs for both ϵ_1 and ϵ_2, which are now very close to experiment in the whole energy range under study (from 2.5 to 6 eV). As for the ratio ζ_2, we find: $\zeta_2^{JGMs} \sim 1.5$, $\zeta_2^{JGM-G} \sim 1.1$, and $\zeta_2^{exp} \sim 1.1$.

The excellent performance of our kernel JGM-G proves the important role that the density gradient ∇n plays in the construction of the XC kernel. We note, however, that while the introduction of the density gradient in ground-state calculations is now usual practice, the density gradient has not been often used in the development of TDDFT XC kernels [74]. An exception is the TDCDFT Vignale-Kohn XC functional [35,75,76]. Silicon has a huge variety of optical applications, from infrared systems [72] to various solar cell devices [77].

F. Gallium arsenide (GaAs)

The results we have obtained for GaAS are shown in Fig. 7. In this case the ratio ζ_2 is found to be more accurate when the kernel JGMs is used: $\zeta_2^{JGMs} \sim 1.2$, $\zeta_2^{JGM-G} \sim 1.4$, and $\zeta_2^{exp} \sim 1.2$.

As for the energy at which $\epsilon_1(\omega) = 0$, both JGMs and JGM-G calculations are slightly blueshifted by 0.1 eV and 0.2 eV, respectively, with respect to experiment. Nevertheless, both kernels yield a realistic description of ϵ_1 and ϵ_2 that is comparable to the performance of, for example, the Bootstrap kernel [23]. In the energy range that goes from 2 to 2.5 eV, however, all our computed absorption spectra are smooth, as in the experiment, while the Bootstrap absorption spectrum [23] exhibits a pronounced structure in this region. Gallium arsenide is widely used in infrared devices, laser diodes, solar cells, and optical windows [72,79].

G. Indium phosphide (InP)

The results we have obtained for InP are shown in Fig. 8. In this case, both kernels under study, JGMs and JGM-G, yield a
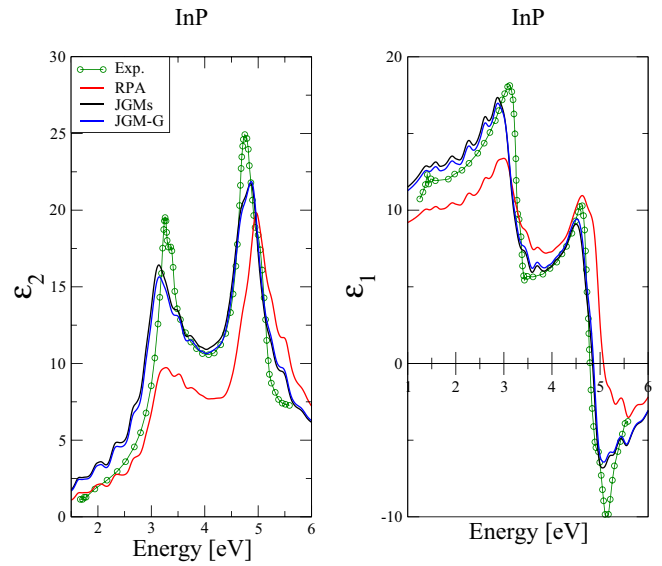

FIG. 8. Same as Fig. 2 but for the InP semiconductor ($E_g = 1.42$ eV [67]). The experimental curves are from Ref. [80] (at $T = 30$ K). The results are obtained with Lorentzian broadening of 0.1.

very accurate description of ϵ_1 and ϵ_2 in close agreement with experiment. InP nanowires are known to have a great potential for optoelectronics [81], and a practical tool such as the simple JGM-G kernel can be of interest in this field.

H. Aluminium arsenide (AlAs)

The results we have obtained for AlAs are shown in Fig. 9. In this case, while RPA calculations largely underestimate the first absorption peak the use of the kernel JGMs largely overestimates this peak. The second absorption peak is also
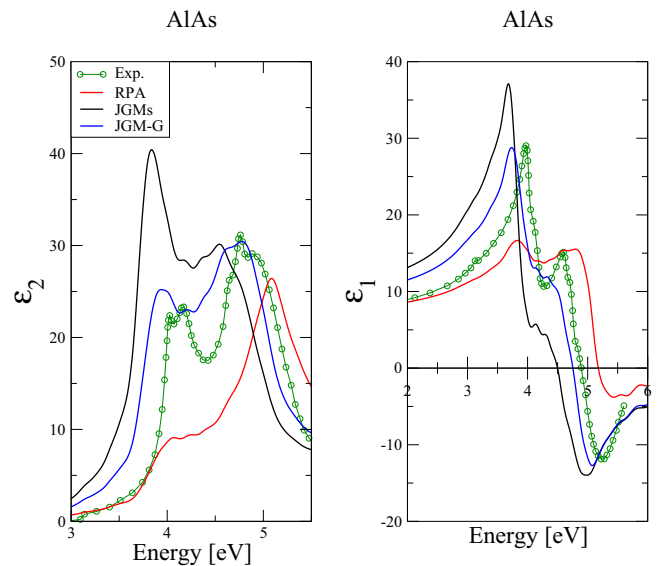

FIG. 9. Same as Fig. 2 but for the AlAs semiconductor ($E_g = 2.24$ eV [82]). The experimental curves are from Ref. [83] (at $T = 95$ K). The results are obtained with Lorentzian broadening of 0.1.
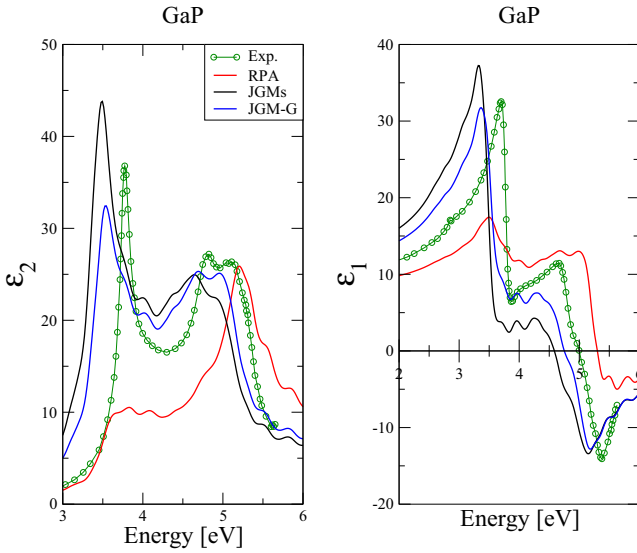
FIG. 10. Same as Fig. 2 but for the GaP semiconductor ($E_g = 2.32$ eV [67]). The experimental curves are from Ref. [64] (for $T = 15$ K). The results are obtained with Lorentzian broadening of 0.1.
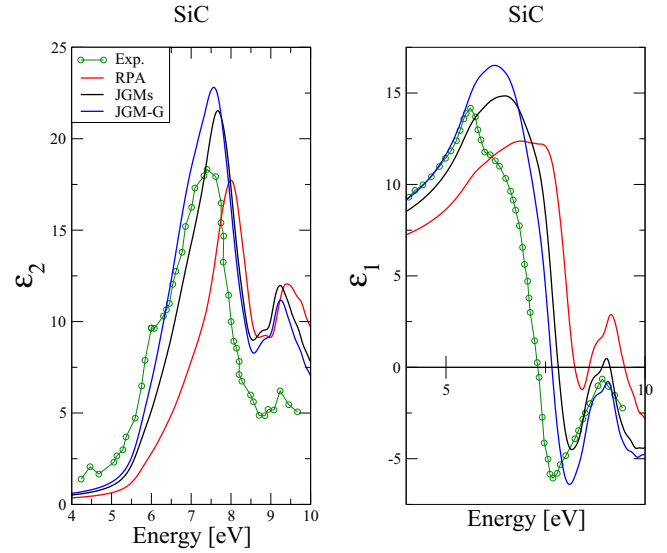

FIG. 11. Same as Fig. 2 but for the SiC semiconductor ($E_g = 2.42$ eV [87]). The experimental curves are from Ref. [38] (at room temperature). The results are obtained with Lorentzian broadening of 0.3.

poorly described by RPA and JGMs: The RPA peak is blueshifted, while the JGMs peak is too shallow and redshifted by about 0.2 eV. The use of our density-gradient-corrected kernel JGM-G, however, yields an excellent description of the experimental optical absorption in the whole energy range under study. Our kernel also considerably improves the ratio ζ_2 over JGMs: $\zeta_2^{\text{JGMs}} \sim 0.8$, $\zeta_2^{\text{JGM-G}} \sim 1.2$, and $\zeta_2^{\text{exp}} \sim 1.4$, and the energy at which $\epsilon_1 = 0$ is considerably better described by the use of JGM-G. AlAs, together with GaAs, is used in excitonic devices, such as the exciton optoelectronic transistor [84].

I. Gallium phosphide (GaP)

In Fig. 10, we show $\epsilon_1(\omega)$ and $\epsilon_2(\omega)$ for GaP. RPA calculations largely underestimate the first absorption peak. The kernels JGMs and JGM-G, however, both yield a reasonably accurate description of the absorption spectra, with $\zeta_2^{\text{JGMs}} \sim 0.6$, and $\zeta_2^{\text{JGM-G}} \sim 0.8$ close to $\zeta_2^{\text{exp}} \sim 0.7$. The energy at which $\epsilon_1 = 0$ is considerably better described with the use of the kernel JGM-G. The second peaks of ϵ_2 and ϵ_1 are also significantly better described by the kernel JGM-G. The nonempirical dynamical polarization functional of TDCDFT [36] was also found to be accurate here. We recall that GaP has been used for photonic-crystal nanocavities, being of interest for integrated, low-power light sources [85] and for submicron-scale optoelectronic devices in the visible [86].

J. Silicon carbide (SiC)

SiC, like AlP and diamond (both considered below), belongs to a class of materials exhibiting a continuum of excitonic effects with no specific peaks. In this case, the excitonic effects are expressed through an increased slope and/or a shoulder just before the main absorption peak. $\epsilon_1(\omega)$ and $\epsilon_2(\omega)$ for SiC are shown in Fig. 11. The best results are clearly obtained with the use of the kernel JGM-G, which significantly

improves, in the whole energy range under study (yielding in particular a slope that is very close to the experimental one), over the use of the kernel JGMs. Moreover, at 9 eV both in the RPA and with the use of the kernel JGMs ϵ_1 is found to be positive, while the use of our kernel JGM-G yields a negative value for ϵ_1 in agreement with the experiment, and also with Bethe-Salpeter calculations (see Fig. 15 of Ref. [38]). SiC is an important wide-band-gap semiconductor that is being used for high-power electronics and photonic devices [88], and SiC nanowires have useful optical properties as well [89].

K. Aluminium phosphide (AlP)

The results we have obtained for AlP are shown in Fig. 12. The experimental absorption spectrum has a main peak at about 4.8 eV, which is strongly underestimated in the RPA and strongly overestimated when the kernel JGMs is used. By using our kernel JGM-G, however, we obtain an absorption spectrum that is in excellent agreement with experiment. An excellent agreement with experiment is also obtained for ϵ_1. While the energy at which $\epsilon_1 = 0$ is blueshifted in the RPA by about 0.5 eV and redshifted with the kernel JGMs by the same quantity (0.5 eV), with the use of our density-gradient-corrected kernel JGM-G ϵ_1 is predicted to be zero at an energy that is very close to the experimental value. Ultrafast exciton dynamics in colloidal AlP nanocrystals were observed recently, showing that these exciton dynamics could be potentially useful for highly efficient optoelectronics materials [91].

L. Diamond (C)

Diamond is one of the most commonly studied and used wide-band-gap solids in optical engineering [92]. The results we have obtained for diamond are shown in Fig. 13. In this case, the kernel JGMs is slightly superior to the kernel JGM-G, but
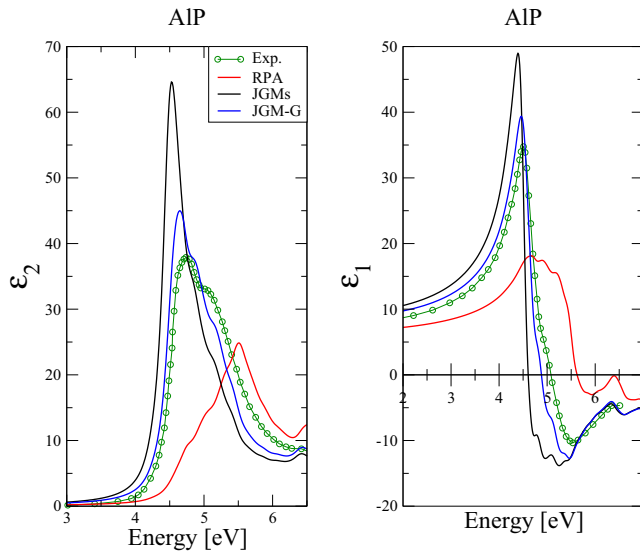
FIG. 12. Same as Fig. 2 but for the AlP semiconductor ($E_g =$ 2.52 eV [82]). The experimental curves are from Ref. [90] (at room temperature). The results are obtained with Lorentzian broadening of 0.1.

both kernels yield a remarkable agreement with experiment for both ϵ_1 and ϵ_2, while RPA calculations are very poor.

M. Wide-band-gap insulators: Magnesium oxide (MgO) and lithium fluoride (LiF)

Here we briefly discuss the optical absorption spectra of two wide-band-gap insulators: MgO and LiF. These are difficult cases for low-cost XC kernels and even for computationally more costly methods, such as the use of the Bethe-Salpeter equation in the context of many-body perturbation theory [39].
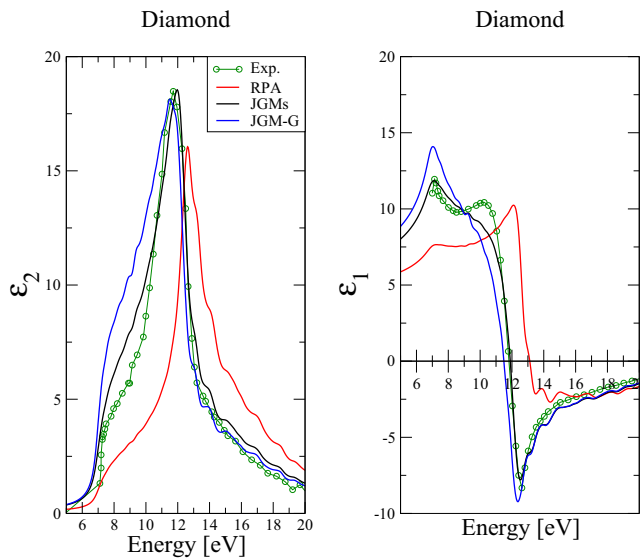

FIG. 13. Same as Fig. 2 but for the diamond wide-gap semiconductor ($E_g = 5.48$ eV [49]). The experimental curves are from Ref. [38]. Temperature effects are almost negligible [65]. The results are obtained with Lorentzian broadening of 0.25.
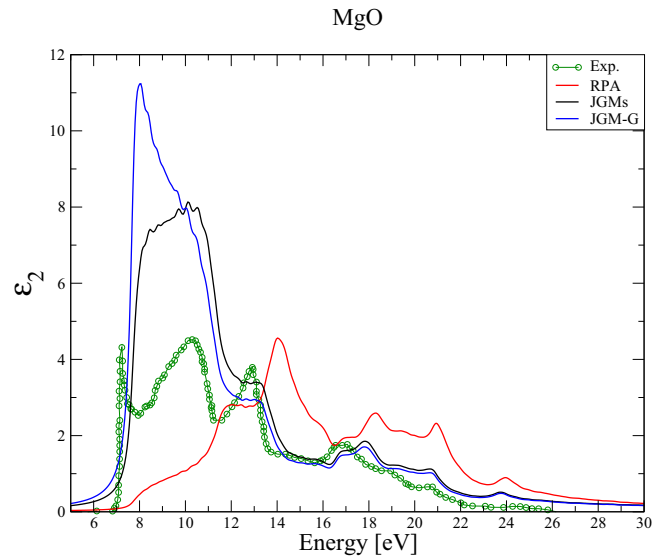

FIG. 14. Optical absorption spectrum of the MgO wide-gap insulator. ($E_g = 7.7$ eV [49]). The experimental data is from Ref. [93] (at room temperature). The results are obtained with Lorentzian broadening of 0.2.

Our main focus here is on excitonic effects, where the jellium-with-gap model proved to be the right model system.

Figure 14 shows the optical absorption spectra we have obtained for MgO. In this case, the use of the kernel JGM-G yields a better description of the first absorption peak, although it is still overestimated. For the second peak, the kernel JGM-G yields a shoulder (instead of a well-defined peak) and the kernel JGMs yields a plateau containing also the first peak. However, the third, fourth, and fifth peaks (at 13 eV, 17 eV, and 21 eV, respectively) closely agree with the corresponding experimental peaks. Noting that the Bootstrap kernel fails for this material [31], we conclude that the use of the kernels JGMs and JGM-G represents a very important step forward.

In Fig. 15, we show the optical absorption spectra we have obtained for LiF. The very-well-defined bound exciton in this material is reasonably well described by using the kernels JGMs and JGM-G, while the RPA fails completely. We note that the overestimated exciton peak that is obtained by using the kernel JGMs is reduced when our density-gradient-corrected kernel JGM-G is used (thus going in the right direction), although at the same time blueshifted by about 0.25 eV.

N. Summary

In Table I, we show various quantities of interest for all materials under study. First of all, we show the fundamental band-gap energy E_g and the maximum value of the density gradient max $|\nabla n|$, which gives us an idea about the electron-density variation in the unit cell. The wide-gap semiconductors (SiC, diamond) and insulators (MgO and LiF) exhibit rapid variations of the electron density, as expected. In the case of regular semiconductors, however, there is no simple relation between E_g and max $|\nabla n|$.

The most important contribution to the absorption spectra is dictated by the head of the matrix kernel, which in the case of a static kernel, such as the kernels considered here, is of
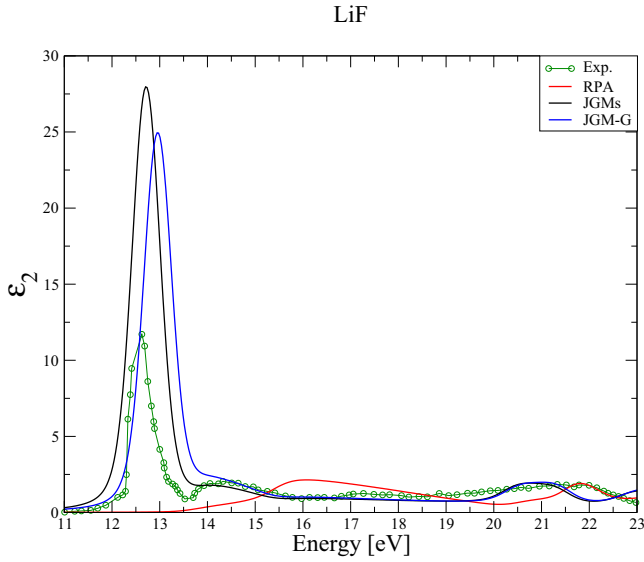
FIG. 15. Optical absorption spectrum of the LiF wide-gap insulator. ($E_g = 13.6$ eV [94]). The experimental data is from Ref. [20] (at room temperature). The results are obtained with Gaussian broadening of 0.25.

the form α/q^2. As in Ref. [33], we extract the parameter α for JGMs and JGM-G: α_{JGMs} and α_{JGM-G}. These results are also reported in Table I.

In Table II we report the parameter ζ_2 [see Eq. (18)] for nine low and medium band-gap materials. These values are rather insensitive to the broadening, thus providing a fair comparison between different approaches. The error statistics (MAE and MARE) exhibit a significant overall improvement when the kernel JGM-G is used (instead of the kernel JGMs).

Next, we analyze the impact of crystal local-field effects (LFE). We note that in the present TDDFT calculations of the density-response matrix one can separate the crystal local-field effects coming from the nonhead elements of the noninteracting Kohn-Sham density-response matrix and the

TABLE I. The band gap energies (in eV), the maximum value of $|\nabla n|$ in the unit cell, the extracted JGMs and JGM-G LRC parameters (α_{JGMs} and α_{JGM-G}). In order to compare α_{JGMs} and α_{JGM-G}, we show in bold the values that corresponds to better agreement with experiment.

	E_g (eV)	max $|\nabla n|$	α_{JGMs}	α_{JGM-G}
InSb	0.23	0.064	**−0.009**	**−0.009**
InAs	0.43	0.092	**−0.03**	**−0.03**
Ge	0.74	0.071	**−0.06**	**−0.06**
GaSb	0.81	0.065	**−0.09**	**−0.09**
Si	1.17	0.083	−0.12	**−0.19**
GaAs	1.42	0.096	**−0.22**	−0.16
InP	1.42	0.134	**−0.27**	−0.24
AlAs	2.24	0.097	−0.52	**−0.37**
GaP	2.32	0.138	**−0.51**	−0.42
SiC	2.42	0.51	−0.25	**−0.39**
AlP	2.52	0.14	−0.6	**−0.48**
Diam	5.48	0.509	**−0.68**	−0.87
MgO	7.7	2.046	−3.36	**−3.96**
LiF	13.6	3.768	**−7.81**	−8.0

TABLE II. The ratio ζ_2 [see Eq. (18)] for experiment (ζ_2^{exp}), RPA (ζ_2^{RPA}), JGMs (ζ_2^{JGMs}), and JGM-G (ζ_2^{JGM-G}) for nine low and medium band-gap materials. The last lines show the mean absolute errors (MAE) and the mean absolute relative errors (MARE).

	ζ_2^{exp}	ζ_2^{RPA}	ζ_2^{JGMs}	ζ_2^{JGM-G}
InSb	1.2	1.4	1.3	1.3
InAs	1.4	1.7	1.6	1.6
Ge	1.3	1.6	1.4	1.4
GaSb	1.2	1.4	1.2	1.2
Si	1.1	2.2	1.5	1.1
GaAs	1.2	1.9	1.2	1.4
InP	1.3	2.0	1.3	1.4
AlAs	1.4	2.9	0.8	1.2
GaP	0.7	2.5	0.6	0.8
MAE		0.8	0.17	**0.11**
MARE (%)		72.7	13.8	**9.2**

crystal local-field effects coming from the nonhead elements of the f_{xc}^{JGM-G} matrix. In this analysis, we always include the crystal local-field effects coming from the nonhead elements of the noninteracting Kohn-Sham density-response matrix and we focus on the impact of crystal local-field effects coming from the nonhead elements of the f_{xc}^{JGM-G} matrix. In Fig. 16, we plot the results we obtain for the optical absorption of Si when (i) only the head ($\mathbf{G} = \mathbf{G}' = \mathbf{0}$) of the f_{xc}^{JGM-G} matrix is considered (blue line), (ii) all (and only) the diagonal elements ($\mathbf{G} = \mathbf{G}'$) of the f_{xc}^{JGM-G} matrix are considered (red line), and (iii) the full f_{xc}^{JGM-G} matrix is included (black line). We clearly see that due to the presence of crystal local-field effects the excitonic peak is brought closer to experiment. We also see that crystal local-field effects are nearly fully incorporated by simply taking the nonhead diagonal elements of the f_{xc}^{JGM-G} matrix, the impact of the nondiagonal elements (the wings) being small.
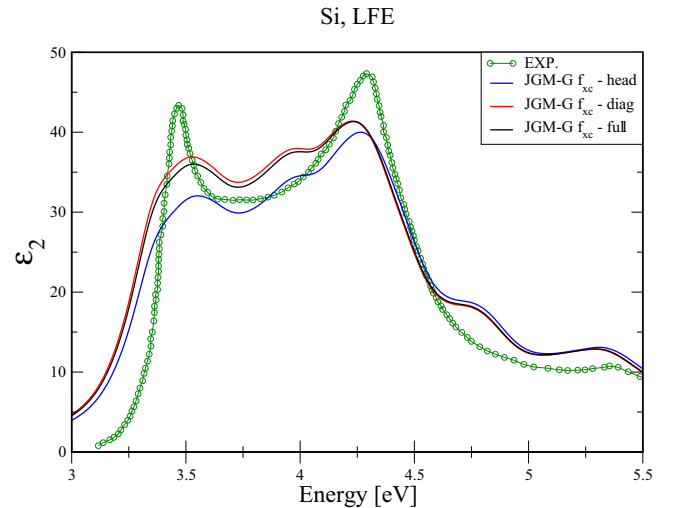

FIG. 16. Optical absorption spectra ϵ_2 of Si, using the full JGM-G matrix kernel (black line), the head of the kernel matrix $\mathbf{G} = \mathbf{G}' = 0$ (blue line), and the diagonal part $\mathbf{G} = \mathbf{G}'$ (red line) compared with experiment (green circles).
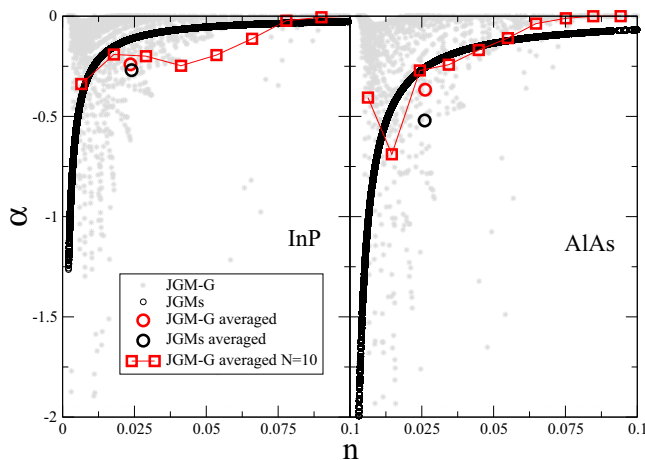
FIG. 17. The $\alpha(\mathbf{r})$ values as a function density $n(\mathbf{r})$ in the unit cell, for InP (left panel) and AlAs (right panel). The total JGMs averaged values are represented by black circles ($< \alpha > = -0.27$ for InP and $< \alpha > = -0.52$ for AlAs). The total JGM-G averaged values are represented by big bold red circles ($< \alpha > = -0.24$ for InP and $< \alpha > = -0.37$ for AlAs). The red squares show the averaged values of $\alpha_{\text{JGM-G}}(\mathbf{r})$ over 10 equidistant density intervals.

Finally in Fig. 17 we show $\alpha(\mathbf{r}) = -G^2/n(\mathbf{r})$, where $G = E_g$ for JGMs and $G = G(n(\mathbf{r}), \nabla(\mathbf{r}))$ for JGM-G [see Eq. (12)]. While $\alpha_{\text{JGMs}}(\mathbf{r})$ is a well-defined function of the density, $\alpha_{\text{JGM-G}}(\mathbf{r})$ has multiple values for a given density, because of the ∇n dependence. When averaging $\alpha_{\text{JGM-G}}(\mathbf{r})$ over 10 equidistant density intervals, one observes that the main contribution to the optical absorption is shifted to densities that are higher than in the case of the kernel JGMs. This represents a crucial difference between these two kernels and shows the novelty of our kernel JGM-G.

V. CONCLUSIONS

We have constructed an XC kernel (named JGM-G), by incorporating the density gradient as an ingredient, with the purpose of providing a low-cost, practical tool for the computation of the optical properties of semiconductors and insulators. We have tested this kernel on a large variety of semiconductors: low-band-gap semiconductors (InSb, InAs, and Ge) exhibiting discrete excitonic effects, regular semiconductors (GaSb, Si, GaAs, InP, AlAs, and GaP) showing enhanced optical properties of great technological interest, and wide-band-gap semiconductors (SiC, AlP, and diamond) characterized by continuous excitonic effects. For all these bulk materials, the JGM-G kernel yields accurate results, in general very close to experiment even when kernels like JGMs, not containing the density gradient as an ingredient, fail.

The JGM-G kernel improves with respect to the original kernel JGM of Ref. [33] and the simplified kernel JGM (JGMs) proposed in Ref. [46]. Particularly important are the results we have obtained for AlAs, GaP, and AlP, where the original kernel JGM (and also JGMs) clearly overestimates the excitonic effects, and also for Si and SiC, where the original kernel JGM (and also JGMs) clearly underestimates the excitonic effects. In all these cases, the incorporation of the density gradient as an ingredient leads to the kernel JGM-G, which is remarkably accurate for the description of the optical absorption.

Our kernel JGM-G corrects the wrong long-range part of the original JGM (and also JGMs) kernel, as seen in the case of jellium spheres, and this explains the good behavior of JGM-G for the description of optical properties in a variety of semiconductors. We recall that the density gradient ∇n has played a major role in the DFT description of ground-state properties of materials, and we expect it to also play a major role in the TDDFT description of the electronic response of a great variety of metals, semiconductors, and insulators. Furthermore, other possible gradient-dependent improvements of the original JGM should not be ruled out.

[1] E. K. U. Gross, J. F. Dobson, and M. Petersilka, *Density Functional Theory II* (Springer, Berlin, 1996), pp. 81–172.
[2] J. Harris and A. Griffin, Phys. Rev. B **11**, 3669 (1975).
[3] D. C. Langreth and J. P. Perdew, Phys. Rev. B **15**, 2884 (1977).
[4] J. M. Pitarke and A. G. Eguiluz, Phys. Rev. B **57**, 6329 (1998).
[5] J. M. Pitarke and A. G. Eguiluz, Phys. Rev. B **63**, 045116 (2001).
[6] L. Schimka, J. Harl, A. Stroppa, A. Grüneis, M. Marsman, F. Mittendorfer, and G. Kresse, Nat. Mater. **9**, 741 (2010).
[7] J. F. Dobson and J. Wang, Phys. Rev. Lett. **82**, 2123 (1999).
[8] S. Lebègue, J. Harl, T. Gould, J. G. Ángyán, G. Kresse, and J. F. Dobson, Phys. Rev. Lett. **105**, 196401 (2010).
[9] J. Harl and G. Kresse, Phys. Rev. B **77**, 045136 (2008).
[10] P. D. Mezei, G. I. Csonka, A. Ruzsinszky, and J. Sun, J. Chem. Theory Comput. **11**, 360 (2014).
[11] L. A. Constantin and J. M. Pitarke, Phys. Rev. B **83**, 075116 (2011).
[12] J. Harl and G. Kresse, Phys. Rev. Lett. **103**, 056401 (2009).
[13] J. Harl, L. Schimka, and G. Kresse, Phys. Rev. B **81**, 115126 (2010).
[14] L. A. Constantin, J. P. Perdew, and J. M. Pitarke, Phys. Rev. Lett. **101**, 016406 (2008).
[15] L. A. Constantin, Phys. Rev. B **93**, 121104 (2016).
[16] F. Furche, Phys. Rev. B **64**, 195120 (2001).
[17] A. Ruzsinszky, J. P. Perdew, and G. I. Csonka, J. Chem. Theory Comput. **6**, 127 (2010).
[18] M. Fuchs, Y.-M. Niquet, X. Gonze, and K. Burke, J. Chem. Phys. **122**, 094116 (2005).
[19] B. Xiao, J. Sun, A. Ruzsinszky, and J. P. Perdew, Phys. Rev. B **90**, 085134 (2014).
[20] A. Marini, R. Del Sole, and A. Rubio, Phys. Rev. Lett. **91**, 256402 (2003).

[21] F. Sottile, V. Olevano, and L. Reining, Phys. Rev. Lett. **91**, 056402 (2003).

[22] G. Onida, L. Reining, and A. Rubio, Rev. Mod. Phys. **74**, 601 (2002).

[23] S. Sharma, J. K. Dewhurst, A. Sanna, and E. K. U. Gross, Phys. Rev. Lett. **107**, 186401 (2011).

[24] V. Turkowski, A. Leonardo, and C. A. Ullrich, Phys. Rev. B **79**, 233201 (2009).

[25] Z. H. Yang and C. A. Ullrich, Phys. Rev. B **87**, 195204 (2013).

[26] M. Dvorak, S.-H. Wei, and Z. Wu, Phys. Rev. Lett. **110**, 016402 (2013).

[27] S. Botti, A. Fourreau, F. Nguyen, Y.-O. Renault, F. Sottile, and L. Reining, Phys. Rev. B **72**, 125203 (2005).

[28] Z. H. Yang, F. Sottile, and C. A. Ullrich, Phys. Rev. B **92**, 035202 (2015).

[29] S. Rigamonti, S. Botti, V. Veniard, C. Draxl, L. Reining, and F. Sottile, Phys. Rev. Lett. **114**, 146402 (2015).

[30] Y.-M. Byun and C. A. Ullrich, Computation **5**, 9 (2017).

[31] Y.-M. Byun and C. A. Ullrich, Phys. Rev. B **95**, 205136 (2017).

[32] V. U. Nazarov and G. Vignale, Phys. Rev. Lett. **107**, 216402 (2011).

[33] P. E. Trevisanutto, A. Terentjevs, L. A. Constantin, V. Olevano, and F. Della Sala, Phys. Rev. B **87**, 205143 (2013).

[34] M. van Faassen, P. L. de Boeij, R. van Leeuwen, J. A. Berger, and J. G. Snijders, Phys. Rev. Lett. **88**, 186401 (2002).

[35] P. L. De Boeij, F. Kootstra, J. A. Berger, R. Van Leeuwen, and J. Snijders, J. Chem. Phys. **115**, 1995 (2001).

[36] J. A. Berger, Phys. Rev. Lett. **115**, 137402 (2015).

[37] L. Reining, V. Olevano, A. Rubio, and G. Onida, Phys. Rev. Lett. **88**, 066404 (2002).

[38] S. Botti, F. Sottile, N. Vast, V. Olevano, L. Reining, H.-C. Weissker, A. Rubio, G. Onida, R. Del Sole, and R. W. Godby, Phys. Rev. B **69**, 155112 (2004).

[39] N. T. Maitra, J. Chem. Phys. **144**, 220901 (2016).

[40] G. Giuliani and G. Vignale, *Quantum Theory of the Electron Liquid* (Cambridge University Press, Cambridge, 2005).

[41] G. Vignale and W. Kohn, Phys. Rev. Lett. **77**, 2037 (1996).

[42] G. Vignale and W. Kohn, *Electronic Density Functional Theory* (Springer, New York, 1998), pp. 199–216.

[43] L. A. Constantin and J. M. Pitarke, Phys. Rev. B **75**, 245127 (2007).

[44] Z. H. Levine and S. G. Louie, Phys. Rev. B **25**, 6310 (1982).

[45] J. P. Perdew and Y. Wang, Phys. Rev. B **45**, 13244 (1992).

[46] C. E. Patrick and K. S. Thygesen, J. Chem. Phys. **143**, 102802 (2015).

[47] C. Ambrosch-Draxl and J. O. Sofo, Comput. Phys. Commun. **175**, 1 (2006).

[48] J. Xia and E. A. Carter, Phys. Rev. B **91**, 045124 (2015).

[49] F. Tran and P. Blaha, Phys. Rev. Lett. **102**, 226401 (2009).

[50] A. V. Krukau, G. E. Scuseria, J. P. Perdew, and A. Savin, J. Chem. Phys. **129**, 124103 (2008).

[51] J. Toulouse, A. Savin, and C. Adamo, J. Chem. Phys. **117**, 10465 (2002).

[52] E. Fabiano, P. E. Trevisanutto, A. Terentjevs, and L. A. Constantin, J. Chem. Theory Comput. **10**, 2016 (2014).

[53] M. Levy, J. P. Perdew, and V. Sahni, Phys. Rev. A **30**, 2745 (1984).

[54] T. Olsen and K. S. Thygesen, Phys. Rev. Lett. **112**, 203001 (2014).

[55] T. Olsen and K. S. Thygesen, Phys. Rev. B **88**, 115131 (2013).

[56] T. Olsen and K. S. Thygesen, Phys. Rev. B **86**, 081103 (2012).

[57] E. Engel, *A Primer in Density Functional Theory* (Springer, New York, 2003), pp. 56–122.

[58] E. Engel and S. H. Vosko, Phys. Rev. A **47**, 2800 (1993).

[59] P. Giannozzi, S. Baroni, N. Bonini, M. Calandra, R. Car, C. Cavazzoni, D. Ceresoli, G. L. Chiarotti, M. Cococcioni, I. Dabo *et al.*, J. Phys.: Condens. Matter **21**, 395502 (2009).

[60] A. Marini, C. Hogan, M. Grüning, and D. Varsano, Comput. Phys. Commun. **180**, 1392 (2009).

[61] A. Sasaki, M. Nishiuma, and Y. Takeda, Jpn. J. Appl. Phys. **19**, 1695 (1980).

[62] P. Lautenschlager, M. Garriga, L. Vina, and M. Cardona, Phys. Rev. B **36**, 4821 (1987).

[63] L. Vinna, S. Logothetidis, and M. Cardona, Phys. Rev. B **30**, 1979 (1984).

[64] S. Zollner, M. Garriga, J. Kircher, J. Humlicek, M. Cardona, and G. Neuhold, Phys. Rev. B **48**, 7915 (1993).

[65] R. Roberts and W. Walker, Phys. Rev. **161**, 730 (1967).

[66] S. Logothetidis, L. Vinna, and M. Cardona, Phys. Rev. B **31**, 947 (1985).

[67] C. Kittel, *Introduction to Solid State Physics, 6th ed.* (Maruzen, Tokyo, 1986).

[68] S. Adachi, Phys. Rev. B **35**, 7454 (1987).

[69] K. Hulme and J. Mullin, Solid-State Electron. **5**, 211 (1962).

[70] D. E. Aspnes and A. A. Studna, Phys. Rev. B **27**, 985 (1983).

[71] A. Milnes and A. Polyakov, Mater. Sci. Eng., B **18**, 237 (1993).

[72] A. Rogalski, Prog. Quantum Electron. **27**, 59 (2003).

[73] S. Zollner, M. Garriga, J. Humlicek, S. Gopalan, and M. Cardona, Phys. Rev. B **43**, 4349 (1991).

[74] A. Ruzsinszky, L. A. Constantin, and J. M. Pitarke, Phys. Rev. B **94**, 165155 (2016).

[75] J. A. Berger, P. L. de Boeij, and R. van Leeuwen, Phys. Rev. B **71**, 155104 (2005).

[76] J. A. Berger, P. Romaniello, R. van Leeuwen, and P. L. de Boeij, Phys. Rev. B **74**, 245117 (2006).

[77] M. A. Green, *Third Generation Photovoltaics: Advanced Solar Energy Conversion*, Springer Series in Photonics Vol. 12 (Springer-Verlag, Berlin Heidelberg, 2006).

[78] P. Lautenschlager, M. Garriga, S. Logothetidis, and M. Cardona, Phys. Rev. B **35**, 9174 (1987).

[79] S. J. Moss and A. Ledwith, *Chemistry of the Semiconductor Industry* (Springer Science & Business Media, New York, 1989).

[80] P. Lautenschlager, M. Garriga, and M. Cardona, Phys. Rev. B **36**, 4813 (1987).

[81] J. Wang, M. S. Gudiksen, X. Duan, Y. Cui, and C. M. Lieber, Science **293**, 1455 (2001).

[82] M. Lorenz, R. Chicotka, G. Pettit, and P. Dean, Solid State Commun. **8**, 693 (1970).

[83] M. Garriga, M. Kelly, and K. Ploog, Thin solid films **233**, 122 (1993).

[84] G. Grosso, J. Graves, A. Hammack, A. High, L. Butov, M. Hanson, and A. Gossard, Nat. Photonics **3**, 577 (2009).

[85] K. Rivoire, Z. Lin, F. Hatami, W. T. Masselink, and J. Vučković, Opt. Express **17**, 22609 (2009).

[86] K. Rivoire, A. Faraon, and J. Vuckovic, Appl. Phys. Lett. **93**, 063103 (2008).

[87] D. Bimberg, M. Altarelli, and N. Lipari, Solid State Commun. **40**, 437 (1981).

[88] S. Castelletto, B. Johnson, V. Ivády, N. Stavrias, T. Umeda, A. Gali, and T. Ohshima, Nat. Mater. **13**, 151 (2014).

[89] H.-K. Seong, H.-J. Choi, S.-K. Lee, J.-I. Lee, and D.-J. Choi, Appl. Phys. Lett. **85**, 1256 (2004).

[90] S. Hwang, T. Kim, Y. Jung, N. Barange, H. Park, J. Kim, Y. Kang, Y. Kim, S. Shin, J. Song *et al.*, J. Alloys Compd. **587**, 361 (2014).

[91] E. Busby, A. Thibert, J. Fuzell, D. C. Arrington, A. M. Jawaid, P. T. Snee, and D. S. Larsen, Chem. Phys. Lett. **557**, 129 (2013).

[92] R. P. Mildren, in *Optical Engineering of Diamond*, edited by R. P. Mildren and J. R. Rabeau (Wiley, New York, 2013), Chap. 1, pp. 1–34.

[93] A. Schleife, C. Rödl, F. Fuchs, J. Furthmüller, and F. Bechstedt, Phys. Rev. B **80**, 035112 (2009).

[94] G. Singh and T. Gallon, Solid State Commun. **51**, 281 (1984).